The Journal of Experimental Biology 213, 4043-4054
© 2010. Published by The Company of Biologists Ltd
doi:10.1242/jeb.048017

The effect of fin ray flexural rigidity on the propulsive forces generated by a biorobotic fish pectoral fin

James L. Tangorra[1,*], George V. Lauder[2], Ian W. Hunter[3], Rajat Mittal[4], Peter G. A. Madden[2] and Meliha Bozkurttas[5]

[1]Department of Mechanical Engineering, Drexel University, Philadelphia, PA 19104, USA, [2]Museum of Comparative Zoology, Harvard University, 26 Oxford Street, Cambridge, MA 02138, USA, [3]Department of Mechanical Engineering, MIT, Cambridge, MA 02139, USA, [4]Department of Mechanical Engineering, Johns Hopkins University, 223 Latrobe Hall, 3400 North Charles Street Baltimore, MD 21218-2682, USA and [5]Department of Mechanical and Aerospace Engineering, The George Washington University, Washington, DC 20052, USA

*Author for correspondence (tangorra@coe.drexel.edu)

Accepted 9 September 2010

SUMMARY

A biorobotic pectoral fin was developed and used to study how the flexural rigidities of fin rays within a highly deformable fish fin affect the fin's propulsive forces. The design of the biorobotic fin was based on a detailed analysis of the pectoral fin of the bluegill sunfish (*Lepomis macrochirus*). The biorobotic fin was made to execute the kinematics used by the biological fin during steady swimming, and to have structural properties that modeled those of the biological fin. This resulted in an engineered fin that had a similar interaction with the water as the biological fin and that created close approximations of the three-dimensional motions, flows, and forces produced by the sunfish during low speed, steady swimming. Experimental trials were conducted during which biorobotic fins of seven different stiffness configurations were flapped at frequencies from 0.5 to 2.0 Hz in flows with velocities that ranged from 0 to 270 mm s^{-1}. During these trials, thrust and lift forces were measured, kinematics were recorded in three dimensions, and digital particle image velocimetry was used to evaluate flow hydrodynamics. The results of the trials revealed that slight changes to the fin's mechanical properties or to the operating conditions can have significant impact on the direction, magnitude and time course of the propulsive forces. In general, the magnitude of the 2-D (thrust and lift) propulsive force scaled with fin ray stiffness, and increased as the fin's flapping speed increased or as the velocity of the flow decreased.

Key words: fish, pectoral fin, fin ray, robotics, biomimetics, flexibility.

INTRODUCTION

Fish routinely exhibit a level of agility that far surpasses the level that human-engineered underwater vehicles have been able to achieve (Bandyopadhyay, 2002). Fish such as sunfish, perch and goldfish can hover, swim forwards and backwards, reorient and rotate in place, and do so with apparent ease in both quiescent and turbulent flows (Lauder et al., 2006). There are many reasons why fish are more maneuverable than the systems humans have been able to engineer. Perhaps the most significant, and most simplistic, explanation is that highly maneuverable fish have fins that are very effective at manipulating fluid and producing forces in three dimensions (Lauder et al., 2006; Zhu et al., 2002; Tytell et al., 2008). Although this seems obvious, until recently aspects of fish fins such as the three-dimensional (3-D) kinematics and mechanical properties, the underlying architecture, and the fin's dynamic interaction with the fluid environment have not been extensively studied by engineers or incorporated into designs of underwater vehicles. Fish use several different types of fins that interact with the water and assume 3-D shapes that are not modeled well using two-dimensional (2-D) representations (Tytell et al., 2008). Fish are able to influence the 3-D shape of their fins and the interaction of the fins with the water by modulating the stiffness of individual fin rays. They are also able to drive the fins in different manners to produce the forces required for the type of swimming being conducted (Alben et al., 2007; Wilga and Lauder, 2000). For example, to produce thrust during steady swimming, the pectoral fins of bluegill sunfish (*Lepomis macrochirus* Rafinesque) are very flexible and execute a graceful, periodic motion led by an upper and lower leading edge (Lauder et al., 2006; Tangorra et al., 2007). By contrast, to produce the large lateral forces required for a yaw turn, the fin has a stiffer, impulsive motion that is led by the movement of the ventral edge (Gottlieb et al., 2010). Thus, to engineer fin-based propulsors that generate and direct forces as a fish fin does, the 3-D motions, flexural properties, and fluid mechanics of the biological fin should be examined, and the most important aspects of these features captured in a biorobotic model.

Few experimental studies have considered the impact of a fin's spatially varying flexural properties simultaneously with complex, 3-D kinematics derived directly from biological motions. The effect of flexibility has been studied mainly in flapping foils with 2-D (heaving and pitching) kinematics (Liu and Bose, 1997; Prempraneerach et al., 2003). It has been demonstrated numerically (Mittal et al., 2006; Zhu and Shoele, 2008) and experimentally (McHenry, 1995; Triantafyllou et al., 2005; Fish et al., 2006; Lauder et al., 2006; Lauder and Madden, 2007) that flexibility is instrumental to the production of propulsive forces and to the efficiency of flapping locomotion. When properly set along the chord and the span, passive flexibility improves propulsive efficiency, and under the correct operating conditions can increase peak thrust and lift forces. Several robotic fins have been developed that used fin-ray-like structures and webbing to create fin kinematics (e.g. Low and Willy, 2006; Low, 2009; Palmisano et al., 2007). For the most

part, these efforts have relied upon mechanisms to prescribe curvatures for relatively stiff fins and have not studied the interaction of highly deformable fin rays and the water. Deformable fins with complex kinematics have been studied primarily numerically. These include analyses of the forces and flows created by the pectoral fins of the bird wrasse (Ramamurti et al., 2002) and of the bluegill sunfish (Mittal et al., 2006). Recently, Zhu and Shoele (Zhu and Shoele, 2008) conducted numerical studies in which the motions of a model of a fin away from the base were not prescribed, but were determined using an iterative fluid-structural interaction. In these studies, the motions of the fin ray bases in a caudal fin and a pectoral fin (Shoele and Zhu, 2009) were varied, and the forces and flows produced by the fin were predicted. The results indicated that the fin's anisotropic flexibility increases efficiency, reduces lateral forces, and reduces the sensitivity of the forces to changes in kinematic parameters (Zhu and Shoele, 2008).

In this paper we: (1) briefly review sunfish pectoral fin kinematics during steady swimming to provide the context for motion programming of a robotic pectoral fin [also see our previous work on bluegill sunfish locomotion where fin kinematics are discussed in more detail (Lauder et al., 2006; Lauder and Madden, 2007; Mittal et al., 2006; Bozkurttas et al., 2007)]; (2) present the development of a biorobotic fin that models the flexible sunfish pectoral fin during steady swimming; and (3) analyze the effects of fin ray flexural rigidity on the fin's propulsive forces. We show that our biorobotic pectoral fins are able to produce positive thrust – and no drag – throughout the entire fin beat, in a manner similar to the previously demonstrated function of bluegill sunfish pectoral fins during steady locomotion. This is a result of replicating the biological movements most responsible for thrust production, and tuning the stiffness of the rays of the robotic fin to those of the biological fin rays. Experimentation conducted with these fins shows that slight changes to the fin's mechanical properties can have significant impact on the direction, magnitude and time course of the propulsive forces.

MATERIALS AND METHODS

Modal decomposition of biological motions

Owing to the complexity of the motion and anatomy of the sunfish's pectoral fins (Alben et al., 2007; Lauder et al., 2006; Tangorra et al., 2007), it was apparent that the biological system and its movements had to be simplified if biologically relevant forces and flows were to be created using a robotic model of reasonable complexity. To determine which aspects of the movement of the biological fin were most responsible for creating the steady swimming forces, the motions of the fin were decomposed into a set of orthogonal modes using proper orthogonal decomposition (POD). Our previous POD study of natural propulsive motions of the bluegill sunfish pectoral fin were conducted for computational fluid dynamic purposes (Bozkurttas et al., 2006; Bozkurttas et al., 2007; Bozkurttas et al., 2009; Mittal et al., 2006), and were used to compute flow patterns generated by the pectoral fin during steady swimming. The POD analysis was based on digitizing nearly 300 points on the fin surface through time to produce a detailed representation of fin surface deformation (also see Dong et al., 2010). These computational fluid dynamic analyses showed that the majority of the fin's force was created when the sweep of the fin was coupled to a cupping and un-cupping of the fin about its spanwise axis (POD mode 1; Fig. 1), and was enhanced when the fin exhibited a distal-end harmonic associated with flexibility (POD mode 3). Together these two (of 19) modes accounted for 55% of the fin's motion (as measured by percentage variance explained), but produced over 90% of the thrust force. Readers are referred to Bozkurttas et al. (Bozkurttas et al., 2009) and Dong et al. (Dong et al., 2010) for an in-depth comparison of modal and actual motions, and for further details of the POD analysis of fin kinematics. We concluded that it was unnecessary for the robotic fin to recreate all aspects of the biological motion, and instead that the robotic fin should model the movements of POD mode 1 (cupping and sweep) and the distal-end flexibility captured in POD mode 3.

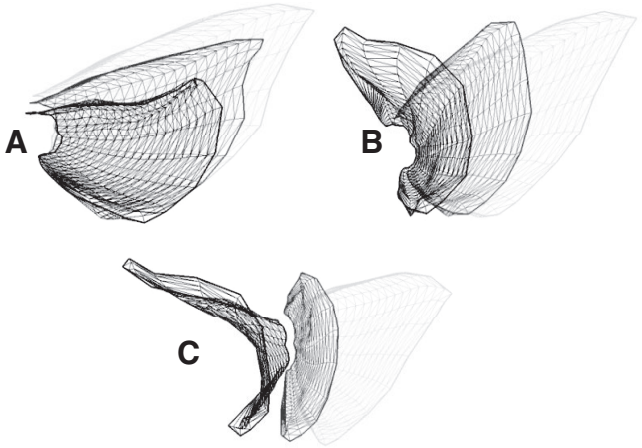

Fig. 1. Mode 1 motion (principal component 1 of a multivariate analysis of pectoral fin kinematics) of the bluegill pectoral fin shown at three time increments during the outstroke. Groupings show fin conformation from lateral (A), 45 deg (B) and 60 deg forward (C). Note the cupping motion in which the dorsal (upper) and lower (ventral) edges begin the fin sweep away from the body, and the change in fin area (about 30% during the outstroke).

Robotic fin construction

The primary design objectives were to create a biorobotic fin that (1) would create biologically realistic motions similar to those exhibited by bluegill sunfish during steady swimming at 0.5–1.5 body lengths s^{-1}, (2) would create propulsive forces like those predicted for POD modes 1 and 3 and measured experimentally on bluegill sunfish, and (3) could be modified to explore the effects of fin kinematics and fin ray stiffness on hydrodynamic forces and flows. This was accomplished by developing a fin that drove independent fin rays with the trajectories of POD mode 1, and that approximated the distal-end flexibility of POD mode 3 by using fin rays with flexural rigidities scaled relative to those of the biological fin rays. A visual comparison of the robotic fin motion to that of a bluegill sunfish is shown in Fig. 2.

The design of the robotic pectoral fin presented in this paper was discussed initially by Tangorra et al. (Tangorra et al., 2008) and is an evolution of the preliminary fin design presented previously (Tangorra et al., 2007). The robotic pectoral fin had five flexible fin rays, of lengths approximately four times those of sunfish, attached to hinges mounted in a curved, rigid base (Fig. 3). From hinge to tip, the length of longest fin ray was 175 mm. The webbings of the fin were made from thin (0.30 mm) polyester (82%) and elastane (18%) weaves (Under Armour, Inc., Baltimore, MD, USA). The curvature of the rigid base, and the angles at which the hinges were set, caused the fin to cup about its spanwise axis as the fin rays were swept forward. Each fin ray was actuated individually by rotational servomotors (HS-645MG, Hitec RCD, Poway, CA, USA) *via* a low-stretch,

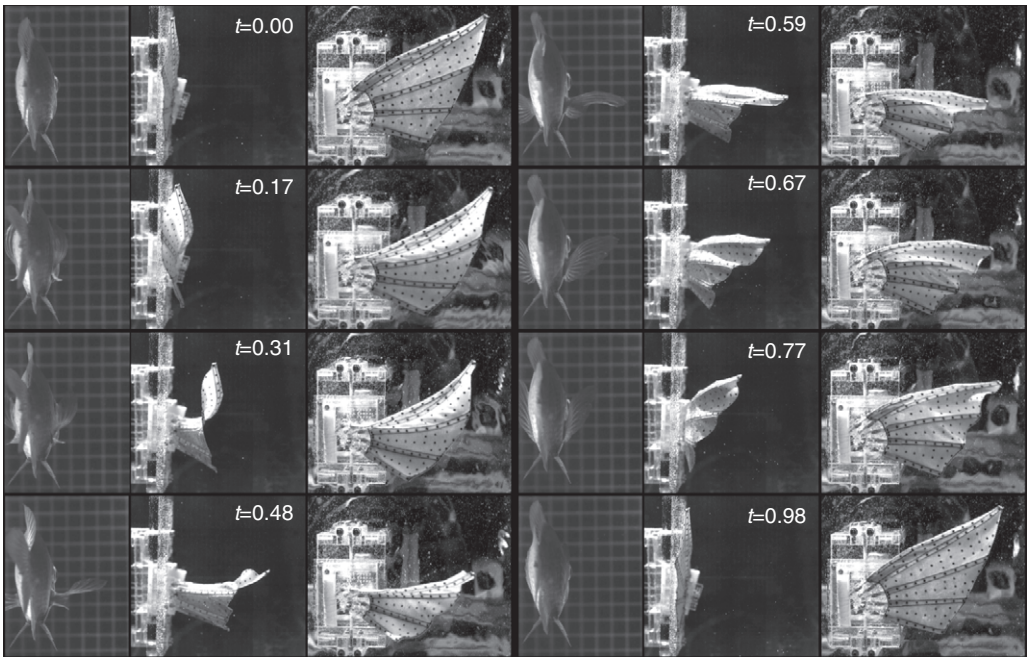

Fig. 2. Comparison of bluegill sunfish pectoral fin motions during steady swimming at 0.5 lengths s^{-1} with those of robotic fin 3 programmed using the primary multivariate kinematic mode 1 (see text for discussion of the kinematic analysis used to program the robotic fin motion). The robotic fin was flapped at 1.0 Hz in a flow of 90 mm s^{-1}. (Left column) Posterior view of bluegill sunfish during steady swimming, with posterior (center column) and lateral (right column) views of a flexible robotic fin (fin stiffness of 1000×). The outstroke occurs from t=0.00 s to just before t=0.59 s. In the lateral view, the robotic fin is moving towards the reader during the outstroke and into the page during the instroke. The length of the longest robotic fin ray is 175 mm. The length of the longest sunfish fin ray is approximately 50 mm.

polyethylene tendon attached to the lower structure of the ray (Fig. 3). The rigid base and flexible fin rays were manufactured using stereo-lithography (Three-Dimensional Systems, Rock Hill, NC, USA) and fused deposition modeling (Stratasys Inc., Eden Prairie, MN, USA).

The geometry of the base of the fin was designed by analyzing the movements of the five biological fin rays (1, 4, 7, 10, 14) that best defined the shape of the sunfish fin throughout POD mode 1 and 3. The other nine rays in the biological fin add to the fin's structure during the fin beat, but are located within areas of the fin where the shape was bounded by the five selected rays, so were omitted to simplify the design and analysis. The positions of 20 points along each of the biological fin rays were tracked and then plotted in 3-D. Near the base, the fin rays remained straight and had a trajectory that could be approximated as the rotation of a line segment in a plane about a point external to the segment. Away from the base, the flexible rays bent and twisted and did not remain aligned with the lower portion of the fin ray. Lines were fitted using least squares to the three points nearest the base of each fin ray at 20 time increments, and the centers of rotation of these lines were found. The rigid base of the robotic fin was then designed so that the hinge for each robotic fin ray would be located at this rotational point and oriented so that the fin ray travelled within a properly oriented rotational plane.

From the fitted lines, the angular rotation of the base of each fin ray was mapped in time, and was fitted using least squares by the Fourier series:

$$\theta(t) = A(0.41 - 0.44\cos(\omega t) - 0.23\sin(\omega t) + 0.03\cos(2\omega t) + 0.08\sin(2\omega t)), \quad (1)$$

where θ is the angular rotation of a specific fin ray, t is time, ω is frequency, and A is a gain set to create the desired rotational displacement. Although each fin ray has a unique trajectory during the complete fin movement (there are 19 total POD modes), the trajectories captured by mode 1 were the same for each fin ray, scaled only in amplitude. These time functions were used to drive the servomotors so that the velocity profile of each fin ray base was correct for the mode 1 movement.

The robotic fin rays were constructed with flexural rigidities – the modulus of elasticity (E) times the area moment of inertia (I) (Gere and Timoshenko, 2004) – that modeled the passive flexural rigidities of the sunfish fin rays. This was done so that the stiffness

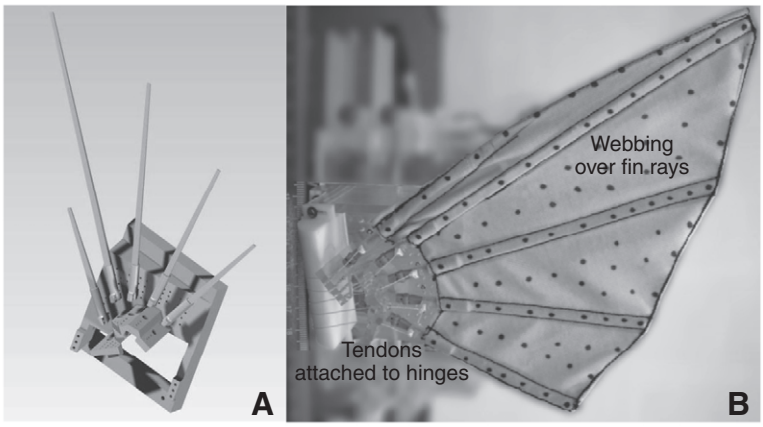

Fig. 3. Design of the biorobotic pectoral fin. (A) CAD image of fin base showing the tapered fin rays without webbing, hinges and the supporting frame. (B) The five-ray biorobotic fin with the nylon tendons and webbing.

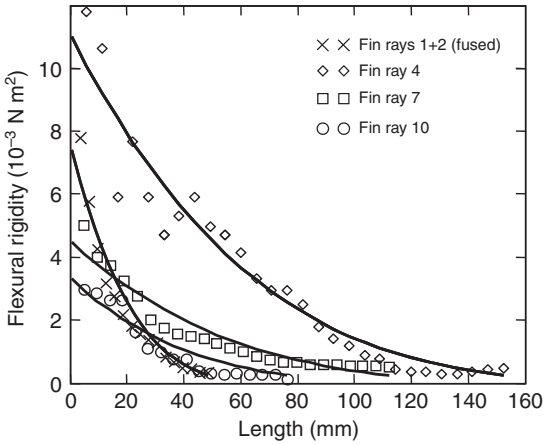

Fig. 4. Flexural rigidity measured for the biological fin rays (points), scaled 1000 times, and fitted by models of fin rays (lines; see text for discussion of how flexural stiffness of the biological fin rays was measured and scaled for the robotic fin) that tapered independently in width and thickness. Note that flexural rigidities of the sunfish fin rays vary considerably along the length of each fin ray and across the fin. Rays 1 and 2 (the dorsal-most rays) are closely attached and were treated as a single element.

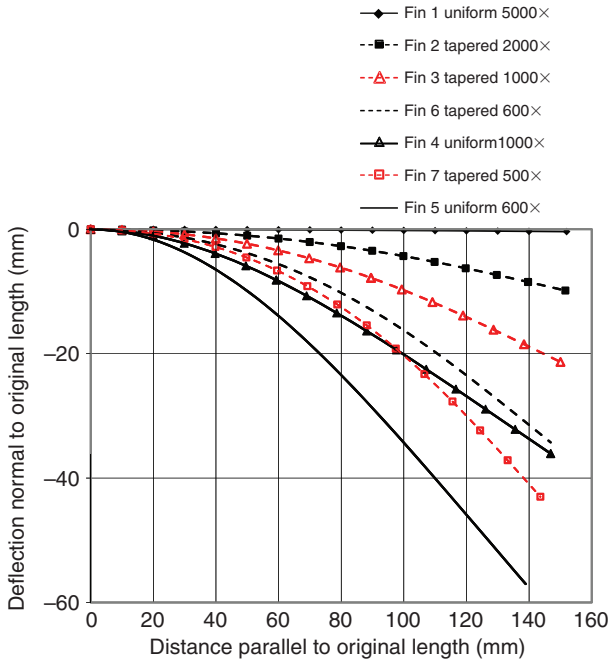

Fig. 5. The curvature and total bending predicted for biorobotic fin ray 4 (152 mm in length) in seven different fin ray models. The bending was estimated in response to a distributed load that increased with the cube of the distance from base. The total load on each fin ray was 0.1 N. The curvature of the tapered fin rays occurred more uniformly along the length of the ray than for the fin rays with the uniform cross section, which bent more significantly near the base.

of the robotic fins would vary across the fin's chord, and from root to tip, in a manner similar to that of the fish fin. Approximate values for the area moment of inertia, flexural stiffness, and modulus of elasticity of the biological fin rays were determined using microtomography and three-point bending tests at several points near the base, middle, and tip of small samples (N=3) of fin rays 1, 2, 5, 6, 8, 11 and 12 (Fig. 4). The flexural rigidity of the biological fin rays is due to passive elastic properties of bone and collagenous intra-ray material, and, as well, to active modulation of the fin rays by the fish (Alben et al., 2007), but for simplicity the robotic fin rays were designed to model only the passive mechanical properties. Active modulation of fin ray shape and stiffness had been investigated previously (Tangorra et al., 2007) so its complexity and the advantages it provided were already recognized.

Because the robotic fins were larger than the fish fins, had fewer fin rays and were to be operated at different flapping speeds and flow rates, the flexural rigidity of each fin ray had to be scaled so that the robotic fin would behave and bend in a manner similar to the fish fin. A first-order estimate of fin-ray bending was made by modeling the fin rays as cantilevers and using the Bernoulli–Euler equation (Ang et al., 1993; Belendez et al., 2002; Gere and Timoshenko, 2004) to express fin-ray deflection in terms of flexural rigidity, fin dimensions and flapping speed. Among other simplifications, beam dynamics were ignored, torsional and lateral loads caused by the webbing between fin rays were ignored, and the bending forces acting on the fin were assumed to be proportional to the square of the fin's velocity. This last assumption treated loading as if it were a drag force, and excluded loading from the 'added mass' of the accelerated water. The fin was assumed to be triangular, with its width increasing linearly along the length. This was considered to be a reasonable approximation of the shape of the fin at any point in the fin beat, although recognized to be a considerable simplification. A scaling rule was then determined which indicated that the fin's deflection, as a fraction of fin ray length, scaled with the square of the fin's flapping frequency (f) and with the length of the fin to the sixth power. Based on typical lengths and flapping frequencies for biological fins, the desired flexural rigidities for the fin rays of a five-rayed biorobotic fin were estimated to be approximately 500–1000 times those of the corresponding biological fin rays.

Fin rays were built with two types of cross sections: (1) rectangular cross sections that tapered in thickness and width from the base to the tip of the fin ray (tapered); and (2) rectangular cross sections that remained uniform along the fin ray's length (uniform). The dimensions of the cross sections were selected by using least squares to fit the flexural rigidities of the robotic rays to those of the biological rays scaled to the desired level (Fig. 4 and Table 1). The tapered rays modeled the scaled flexural rigidity over the length of the fin ray, while the uniform cross section rays modeled the mean flexural rigidity.

The deflection and curvature of a bending fin ray is a function of the scaling factor, loading and how the flexural rigidity varies along the fin ray length (Fig. 5; Table 1) (Gere and Timoshenko, 2004). Therefore, fin rays of different cross section styles that were fitted to the same flexural rigidities had different levels of stiffness [e.g. fin 3 (tapered 1000×) and fin 4 (uniform 1000×); Fig. 5]. Only the tapered cross sections, which had a flexural rigidity that varied in a manner similar to the biological fin rays, were expected to closely follow the scaling law and to exhibit a bending curvature like the biological rays. The rays with uniform cross sections were predicted to bend most near the base, where the ray was anchored, and to be rather straight towards the fin ray tip. By contrast, the tapered rays, which were thicker at the base and thinner at the tip, were predicted to have a more uniform curvature along their length.

Experimentation

The motions, flows and forces produced by robotic fins with seven flexural rigidity (EI) configurations were evaluated. Fin rays with

Table 1. Scaling factors and relative stiffness for each of the seven robotic pectoral fins

Fin	Cross section	Scaling factor	Relative stiffness	Fin ray 4 base (mm)	Fin ray 4 tip (mm)
1	Uniform	5000	1	3.8×2.7	3.8×2.7
2	Tapered	2000	2	3.8×2.9	2.0×1.1
3	Tapered	1000	3	3.8×2.3	1.1×0.9
4	Uniform	1000	5	3.5×1.6	3.5×1.6
5	Uniform	600	7	3.5×1.4	3.5×1.4
6	Tapered	600	4	3.0×2.1	0.9×0.8
7	Tapered	500	6	2.5×2.1	0.9×0.7

The dimensions of the base and tip of fin ray 4 are provided for each of the fins. The changes in the dimensions of fin ray 4 are representative of the geometric changes made to each of the five fin rays as fin stiffness was altered.

tapered cross sections were constructed for scaling factors of 500, 600, 1000 and 2000 times (×) that of the biological fin rays. Fin rays with uniform cross sections were constructed for scaling factors of 600×, 1000× and 5000×. To assess repeatability, several sets of fin rays were built and tested for each of the 500×, 600× and 1000× configurations. The 5000× fin rays were considerably stiffer than the other sets of fin rays, and appeared rigid when moved through the water within a fin. These fin rays were used to investigate whether the kinematics of the cupping and sweep (mode 1) motions alone (Fig. 1) would be sufficient to create thrust during the outstroke, or if it was necessary to have the cupping and sweep motion paired with flexibility.

Fin beats were cycled at frequencies of 0.50, 0.65, 1.00, 1.30 and 1.60 Hz in free stream flows of 0, 90, 180 and 270 mm s^{-1}. A recirculating flow tank was used to create flow past the fin, which was mounted above the tank (described below); this was the same flow tank used for biological studies of bluegill sunfish fin motion (Lauder et al., 2006; Lauder and Madden, 2007; Lauder and Madden, 2008). Fins with tapered fin rays were also tested at 2.00 Hz, but not at all flow rates. These operating conditions corresponded to Reynolds numbers from 0 to 50×10^3, and Strouhal numbers (St) ranging from 0.3 to 3.4 and infinite when the flow rate was zero. This range spanned and exceeded the Strouhal numbers that were used in previous biological studies of bluegill sunfish pectoral fins and computational fluid dynamic analyses (Lauder et al., 2006; Lauder and Madden, 2007; Dong et al., 2010). A full complement of trials was conducted on fins that had tapered fins rays, but fins with uniform cross sections were tested using a reduced, although still broad, set of conditions.

Force measurements

As described previously in Tangorra et al., 2007 (Tangorra et al., 2007), biorobotic fins were supported from a carriage that was mounted to the top of a rectangular flow tank. The carriage rested on eight precision air bearings (New Way S301301, New Way Air Bearings, Aston, PA, USA), and could translate fore, aft and laterally, or be fixed against two s-beam load cells (LSB200, FUTEK Advanced Sensor Technology, Inc., Irvine, CA, USA). This arrangement allowed fin forces to be measured simultaneously along the thrust (anterior–posterior) and lift (dorsal–ventral) axes. The magnitude and direction of the 2-D force was calculated by combining the measured thrust and lift forces vectorially.

Data were collected at 200 Hz using a National Instruments 6062-E data acquisition board (National Instruments Corp., Austin, TX, USA) and low-pass filtered at 10 Hz. The low pass filter was designed using the Kaiser window method to have a pass-band frequency of 10 Hz, a stop-band frequency of 12 Hz, and a peak error of 10^{-4} (Oppenheim and Schafer, 1975). Representative results for the forces produced during the outstroke, instroke and complete stroke cycle of the fin were calculated by averaging forces from six stroke cycles. Standard errors were calculated for each mean force curve.

Kinematic and fluid visualization

High-resolution (1024×1024 pixel), high-speed (250 frames s^{-1}) video and digital particle image velocimetry (DPIV) (Willert and Gharib, 1991) were used to document the kinematics and fluid response for fins with tapered 500×, 600× and 2000× fin rays. Our procedures followed those used in our previous kinematic and fluid dynamic studies as documented by Standen and Lauder (Standen and Lauder, 2005; Standen and Lauder, 2007), Lauder and Madden (Lauder and Madden, 2007), Lauder et al. (Lauder et al., 2007) and Drucker and Lauder (Drucker and Lauder, 2005). Briefly, for kinematic recording of robotic fin motion, three synchronized cameras (Fastcam, Photron USA Inc., San Diego, CA, USA), calibrated in three dimensions using direct linear transformation, and a series of mirrors were arranged to capture the dorsal, lateral and posterior views of the fins simultaneous with the measurement of fin forces. These videos were used to provide an overview of the kinematics of robotic fin motion (e.g. Fig. 2). DPIV was used to capture transverse (chord-wise) slices of the fin and fluid at the root, middle, and distal end of the fin, and longitudinal (span-wise) slices along the dorsal edge, midline and ventral edge of the fin at 500 frames s^{-1}. DPIV particle data were analyzed using DaVis 7.1 software from Lavision Inc. to provide an indication of the vortical patterns associated with robotic fin motion for comparison with previous studies of fluid flows generated by bluegill sunfish pectoral fins during propulsion (Drucker and Lauder, 1999; Lauder et al., 2006; Lauder and Madden, 2007).

RESULTS

Kinematics

The movements of the flexible robotic fins were visually very similar to those of the sunfish fin when the flexural rigidities of the robotic fin rays were scaled between 500 to 1000 times those measured for the biological fin rays (Fig. 2). The lower portions of the fin rays remained straight and followed the mode 1 trajectories that were actuated at the fin ray base. The more distal sections exhibited the complex bending and 3-D curvatures of the biological fin. The flexible fin rays bent and were curved by normal forces from the fluid and lateral forces from the webbing. Owing to differences in the load acting on the fin and the fin's dynamic response and interaction with the water, fin movements were slightly different for each operating condition and fin stiffness. In general, the distal end of the robotic fin bent back during the outstroke as the fin moved into the flow, such that the forward surface of the fin's webbing faced backwards (Fig. 2; t=0.17 s, 0.31 s). The dorsal leading edge of the fin moved forward and down, and by the end of the outstroke the dorsal half of the webbing was nearly horizontal (Fig. 2; t=0.48 s, 0.59 s). The distal end of the fin then straightened and continued to move forward into the flow even after the base of the fin had begun the instroke. As the fin was moved back towards the 'fish' body, the fin opened and the webbing expanded. In contrast to the webbing of the fish fin, which remains relatively smooth throughout the fin beat, the webbing of the robotic fin was looser, and at times created pockets (Fig. 2; t=0.67) or folded upon itself.

The fin that used the most rigid fin rays (5000×) exhibited the mode 1 cupping and sweep motion at the fin base, but, as expected,

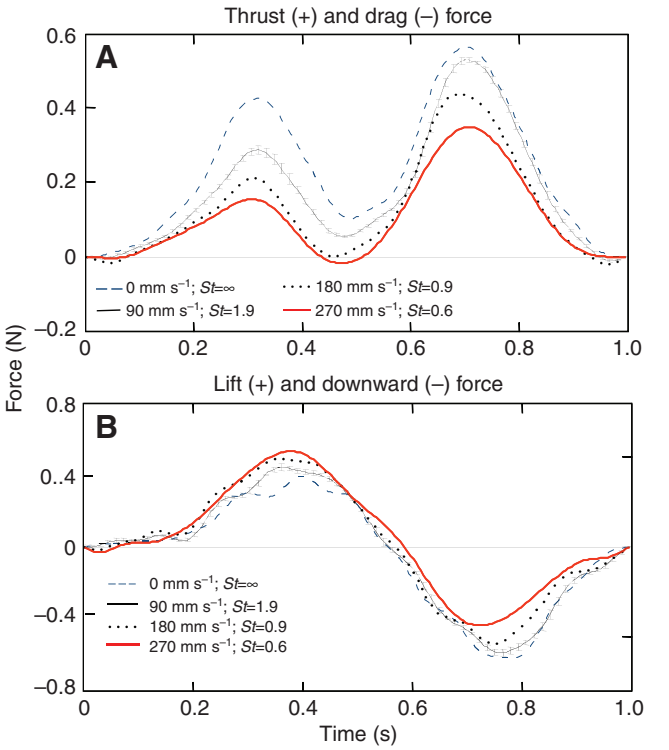

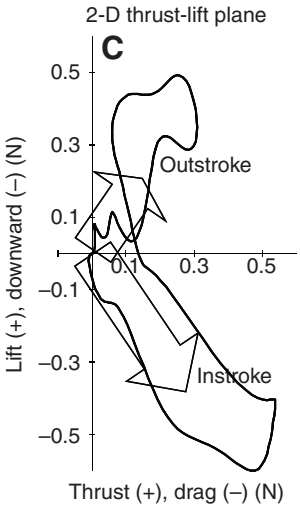

Fig. 6. Robotic fin forces at different flow rates at a flapping frequency of 1.00 Hz. (A) Thrust (+) and drag (–) and (B) lift (+) and downward (–) forces produced by biorobotic fin 3 with a flexural rigidity 1000 times that of the biological fin. (C) The 2-D forces in the thrust–lift plane, with arrows representing magnitude and direction of average force during the outstroke and instroke. For clarity, standard error bars are shown only for the force traces when the fin was operated at 90 mm s^{-1}. These errors are representative of the errors associated with each curve. For clarity, only every third error bar is shown. Note the two thrust peaks (corresponding generally to fin outstroke and instroke), and that at 0 and 90 mm s^{-1} flow speeds, the robotic fin generates thrust only, even during the reversal from outstroke to instroke.

moved stiffly through the water and lacked the dynamic interaction with the water that made the flexible robotic fins bend and twist in a similar manner to the biological fins. The fin with fin rays scaled to 2000× deformed more than the 5000× fin, but its motions still appeared stiff relative to the graceful movements of the biological fins.

Forces

In general, fins with fin rays that had flexural rigidities scaled to 500×, 600× and 1000× produced forces similar in pattern to those measured experimentally (Lauder et al., 2006) and predicted numerically (Dong et al., 2010; Mittal et al., 2006) for the biological pectoral fin. The stiffer fins (2000× and 5000×) did not. Representative forces from the tapered 1000× fin are shown in Figs 6 and 7. Peaks in thrust occurred during both the outstroke and the instroke, and under many conditions thrust was created during the transition from moving into the flow during the outstroke to moving back with the flow and towards the plate that represented the body of the fish. Lift forces correlated primarily with the movement of the dorsal half of the fin. Lift occurred during the outstroke as the upper half of the fin was brought forward and down into the flow, and negative lift (ventral direction) occurred as the fin was brought back. The peak magnitudes of the lift forces were similar to the peak magnitude of the thrust. Exact magnitudes were dependent on operating conditions. When considered in the 2-D thrust–lift plane (Fig. 6C), these forces would drive a fish forward and upward during the fin's outstroke, and then forward and downward during the instroke. Average forces are shown in Fig. 8 for fins flapped at 1.00 Hz in flows from 0 to 270 mm s^{-1}, and in Fig. 9 for fins flapped at frequencies from 0.50 Hz to 1.60 Hz in flows of 90 mm s^{-1}. The trends depicted are representative of the trends observed at other operating conditions.

Unlike the more flexible fins, the stiffer fins (2000× and 5000×) produced drag, not thrust, during the outstroke. Lift forces were similar to those from the flexible fins: lift during the outstroke, and thrust and negative lift during the instroke. The forces produced by these stiffer fins were similar to those reported for the robotic pectoral by Tangorra et al. (Tangorra et al., 2007).

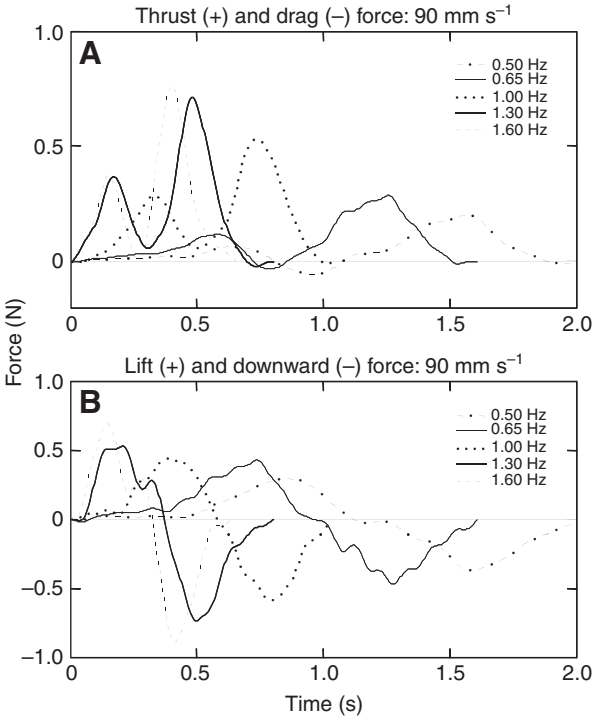

Fig. 7. Fin force patterns through time vary with fin-beat frequency. Thrust (+) and drag (–) and (B) lift (+) and downward (–) forces for robotic fin 3 with tapered 1000× fin rays, plotted against absolute time. The fin was tested at a flow rate of 90 mm s^{-1} at different flapping frequencies. Note the increase in thrust with frequency, and absence of a drag phase during outstroke–instroke reversal for the two highest frequencies.

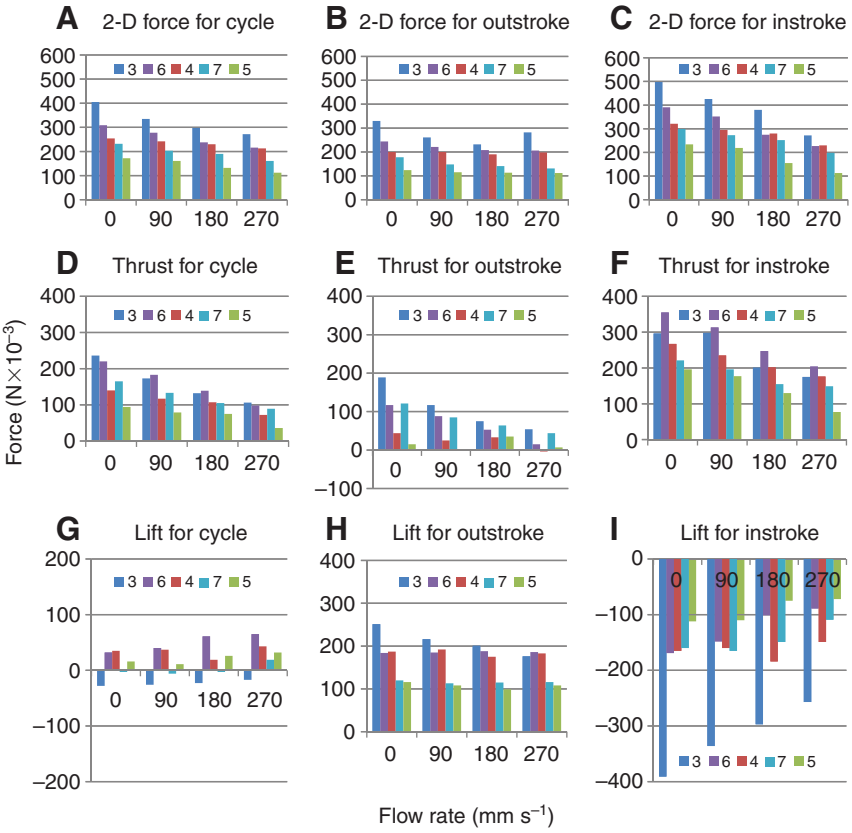

Fig. 8. Average forces for fins with fin rays of different stiffness at a fin-beat frequency of 1.00 Hz, and flow rates of 0, 90, 180, and 270 mm s^{-1}. Fins are depicted in the order of decreasing stiffness: 3 (blue, tapered 1000×), 6 (purple, tapered 600×), 4 (red, uniform 1000×), 7 (light blue, tapered 500×), and 5 (green, uniform 600×). Averages are shown for the 2-D force vector (top row), and for the thrust (middle row) and lift (bottom row) components over the full cycle (left column), the outstroke (middle column), and the instroke (right column). Standard errors ranged from 1 to 9 mN and are not depicted; in most cases, standard error bars were too small to see clearly.

The forces generated by each of the five flexible fins (tapered and uniform 1000×, tapered and uniform 600×, and tapered 500×) were dependent on the speed of the free-stream flow (U) and on the frequency at which the fin was flapped (f). The basic shapes of the force curves for a particular fin did not change considerably as U and f varied, but the magnitudes of the forces did.

With very few exceptions across all operating conditions, when the frequency at which the fin was flapped was held constant, and the speed of the flow was increased (St decreased), the average magnitude of the 2-D force and the average thrust decreased (Fig. 8, top and middle row). This held over the full fin beat, and during the outstroke and the instroke. Similar trends were exhibited by the lift forces (Fig. 8, bottom row), but the patterns were not as consistent as for the thrust and 2-D forces. The average lift produced by a fin remained relatively constant during the fin's outstroke, whereas the average magnitude of the negative lift during the instroke tended to decrease between the extreme flow speeds of 0 and 270 mm s^{-1}. This led to a general increase in the average lift produced by a fin over the fin beat as the flow speed increased.

When flow speed was held constant and the fin's flapping frequency was increased (St increased) the average magnitude of the 2-D force and thrust generally increased over the full fin beat, and individually during the outstroke and instroke (Fig. 9). The average lift did not necessarily increase over the fin beat, but average lift did increase during the outstroke, and average negative lift increased during the instroke.

The trend of increases in force with higher flapping frequency ended for several fins at the highest frequency (1.60 Hz) tested. For example, fin 4 (uniform 1000×) produced lower average 2-D and thrust forces at 1.60 Hz than at 1.30 Hz (Fig. 9, red), and the rate at which forces increased with frequency decreased for fins 7 (tapered 500×) and 5 (uniform 600×) at the higher flapping speeds. The trend continued for fin 7 at 2.00 Hz. Fins 4 and 5 were not tested at this frequency. It could be seen on the high-speed video that these very flexible fins behaved like low pass systems. At the higher frequencies tested, the distal end of the fin would not move through as large of a displacement as at the lower frequencies, despite the base of the fin rays being actuated through the same full movement. The smaller displacements of the distal end resulted in lower thrust during the outstroke in several cases. The smaller displacement most likely reduced the dimensions of the wake shed by the fin. Therefore, the Strouhal numbers at which these fins were operating were lower than the nominal values calculated using a full fin displacement.

Comparisons were made between fins that produced thrust during the outstroke (fins 3, 4, 5, 6 and 7). The stiff 5000× (fin 1) and 2000× (fin 2) fins produced drag during the outstroke, and were therefore excluded from this analysis. At each operating condition, average values for the thrust, lift and magnitude of the 2-D force vector were determined over the full fin beat, the outstroke, and the instroke. Across all test conditions, with few exceptions, a stiffer fin produced greater average 2-D force than a more compliant fin during the outstroke, the instroke and the entire fin beat. As illustrated in Figs 8 and 9 (plots A–C) the average magnitude of the 2-D force tracked consistently with the stiffness of the fin rays. A few exceptions did occur between fins of similar stiffness. For example, at an operating condition of 1.60 Hz and 90 mm s^{-1} (Fig. 9), fin 4 produced lower average 2-D force than the more compliant fin 7, and at 1.00 Hz and 180 mm s^{-1} (Fig. 8) fin 4 produced greater 2-D force during the instroke than the slightly stiffer fin 6. The pattern of the stiffer fin producing greater force did not hold nearly as consistently for thrust and for lift. Similar trends existed at certain operating conditions and for some fins, but the exceptions to the trend indicate that there is a complex relationship between the stiffness of the fin and the thrust and lift components of the force.

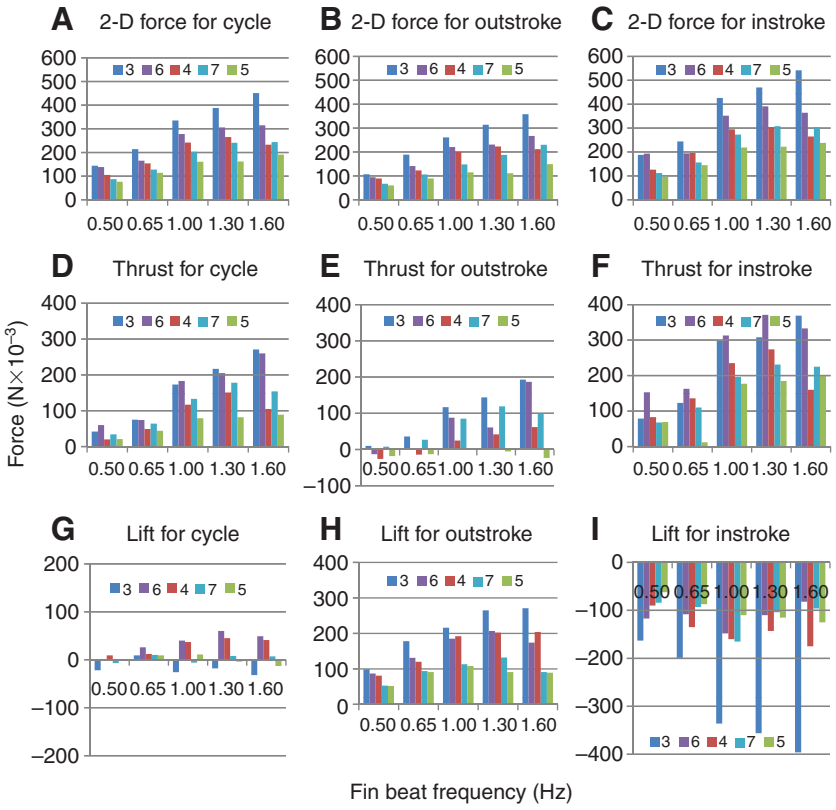

Fig. 9. Average forces for fins with fin rays of different stiffnesses at a flow rate of 90 mm s^{-1} and beat frequencies of 0.50, 0.65, 1.00, 1.30, and 1.60 Hz. Fins are depicted in the order of decreasing stiffness: 3 (blue, tapered 1000×), 6 (purple, tapered 600×), 4 (red, uniform 1000×), 7 (light blue, tapered 500×), and 5 (green, uniform 600×). Averages are shown for the 2-D force vector (top row), and for the thrust (middle row) and lift (bottom row) components over the full cycle (left column), the outstroke (middle column), and the instroke (right column). Standard errors ranged from 1 to 9 mN and are not depicted; in most cases, standard error bars were too small to see clearly.

Over the full fin beat, fins with tapered rays produced greater average thrust than those with uniform cross sections (Figs 8 and 9, plot D). This held true independently of fin stiffness. For example, fin 7 (tapered 500×) was more compliant than fin 4 (uniform 1000×), yet consistently produced significantly more thrust. Fin stiffness had more bearing on average thrust when fins with similar cross section designs (tapered and uniform) were compared. Between the two fins with uniform rays (fins 4 and 5) the stiffer fin always produced an average thrust that was greater than, or equal to, the thrust from the more compliant fin. This was not quite as clear among fins with tapered cross sections. Both fin 6 (tapered 600×) and fin 3 (tapered 1000×) always produced more thrust than fin 7 (tapered 500×), but fin 6 often produced greater average thrust than the stiffer fin 3.

During the outstroke (Figs 8 and 9, plot E), the stiffest of the fins (fin 3) produced the greatest average thrust at all test conditions. The other tapered fins (fins 6 and 7) consistently produced greater thrust than fins with uniform cross section rays (fins 4 and 5), but there was not a consistent order between fins 6 and 7 as to which produced the greater thrust during the outstroke. Among the fins with uniform fin rays, the stiffer fin 4 tended to produce greater thrust than fin 5. In fact, in many instances the very compliant fin 5 produced thrust during only a small portion of the outstroke, and overall generated a net drag during the outstroke (Fig. 9, plot E).

When considering the thrust created during the instroke only (Figs 8 and 9 plot F), if fin 6 is excluded from the comparison, a strong trend is evident where the stiffer fin produced greater thrust than a more compliant fin. This pattern was disrupted by fin 6, which at flapping frequencies below 1.60 Hz, at all flow rates, produced significantly greater thrust during the instroke than all other fins. Fin 3 was stiffer, generated a larger magnitude 2-D force throughout the fin beat than fin 6, and greater thrust during the outstroke, yet fin 6 produced greater thrust during the instroke. This can be seen most clearly by considering the 2-D force vector in the thrust-lift plane. The magnitude of the force produced by fin 6 was lower than that from fin 3, but the force was preferentially directed along the thrust axis.

Over the full fin beat, no strong pattern was evident for the effect of fin stiffness on average lift. The stiffer fins (3, 6, 4) produced greater magnitude lift than the more compliant fins (7, 5), but within these two groups, stiffness did not determine which fin produced greater lift. Patterns were stronger for the lift during the outstroke than for the lift over the full fin beat, but the patterns were not nearly as consistent as for the effect of stiffness on the 2-D force. During the outstroke, the stiffer fins (3, 6, 4) produced significantly more lift than the more compliant fins (7, 5), and within these groups a stiffer fin produced more lift than a more compliant fin. Fin 3 (uniform 1000×) disrupted this pattern at several test conditions and produced slightly greater lift than the stiffer fin 6 (taper 600×). This occurred, for example, at 1.00 Hz and 0 and 90 mm s^{-1}, and at 1.30 Hz and 180 mm s^{-1}. Like for the outstroke, during the instroke the stiffest fin (fin 3) produced a greater average magnitude lift (negative lift) than the other fins. However, among the other fins, the ordering of which fin produced the greater force varied greatly with operating condition. In some cases the average negative lift was ordered with fin stiffness (e.g. 1.00 Hz, 0 mm s^{-1}), while in others, the most compliant fin produced significantly more negative lift than significantly stiffer fins (e.g. 1.60 Hz, 90 mm s^{-1}).

Flow patterns

DPIV analysis of the fluid dynamics of the robotic pectoral fins clearly showed the development of vortices and fluid jets by the fin that qualitatively matched those produced by the sunfish pectoral fin during unrestrained locomotion (Lauder et al., 2006). Most notably, the robotic pectoral fins created the dual leading edge vortices characteristic of bluegill pectoral fins during the outstroke.

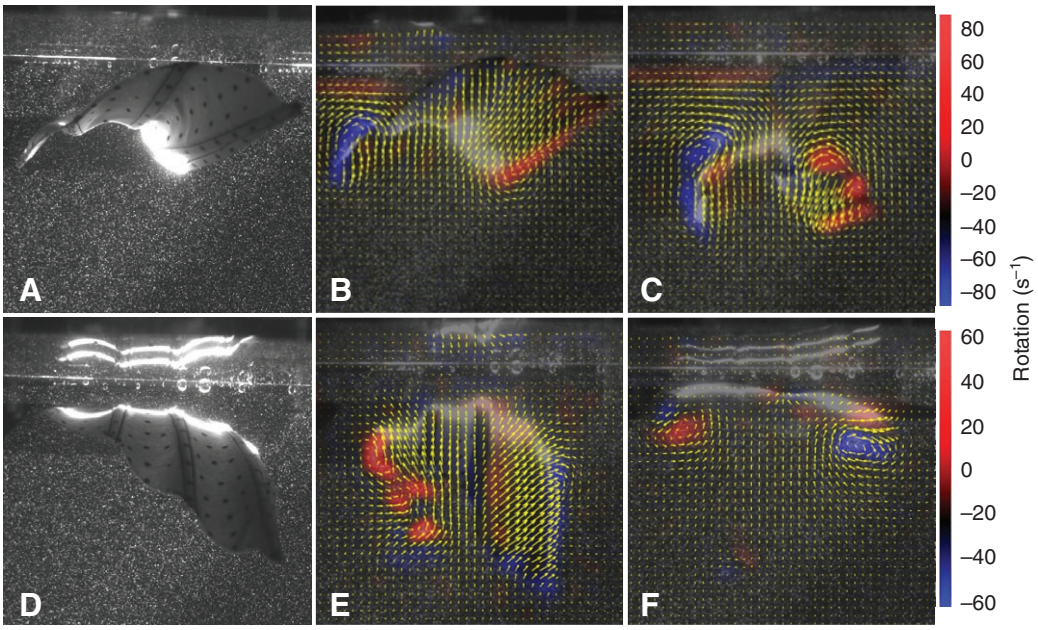

Fig. 10. Robotic pectoral fin imaged in a transverse light sheet (posterior view) for particle image velocimetry of flow patterns produced during the beat. (A,D) Video images of the robotic fin during the outstroke and instroke, respectively. (B,C,E and F) Yellow arrows show absolute flow velocity vectors, and color bar indicates vorticity. The laser light sheet intersects the pectoral fin approximately two-thirds of the way along its length. (B) Leading edge vortices develop on the dorsal (right) and ventral (left) leading edges during the early outstroke. (C) These vortices remain attached throughout the outstroke, and shear layers form on the fin margins. (D,E) Vortices redevelop during the instroke. (F) These vortices are shed into the flow at the end of the instroke. Note the presence of dual leading edge vortices (on both the dorsal and ventral edges). The fin beat frequency was 1.60 Hz, free stream flow was 90 mm s^{-1}, and the fin rays were tapered 500× (fin 7).

Vortices were most clear when analyzed in the transverse plane (perpendicular to sweep of fin; Fig. 10). Vortices developed along the upper and lower leading edges of the fin early in the fin's outstroke. These vortices remained attached, or very close, to the leading edges and grew until they were shed into the flow ipsilaterally, ventrally and backward at the end of the outstroke. Vortices redeveloped along the upper and lower fin edges at the beginning of the instroke, and remained along the fin's edges until the fin neared the body plate and stopped its motion. Both the upper and lower margins of the fin thus developed attached leading-edge vortices. The manner in which the fin pushed the surrounding fluid was most easily analyzed in the lateral plane (from root to tip). As the fin moved away from the body plate during the outstroke, a counter-clockwise vortex was created between the fin and the plate. For fins that created thrust during the outstroke, this relatively large swirl of fluid was pushed into the flow faster than the freestream. The direction of this flow changed during the outstroke, from nearly straight back at the midpoint of the outstroke, to backward and ipsilaterally at the end of the outstroke. For fins that did not create thrust during the outstroke, the swirl of fluid between the fin and the plate was still created, but it moved along with the flow at a rate slower than the freestream. During the fin's instroke, fluid was pushed back into the flow such that by the end of the instroke the direction of the jet, and of the vortices shed from the leading edges, was backward and contra-lateral.

DISCUSSION

Overview of biorobotic fin design and performance

This biorobotic pectoral fin was an effective physical model of the biological fin. It produced biologically relevant forces and flows, and had the degrees of freedom and scalability required to investigate the effects of fin kinematics and structural properties on propulsive forces. The success of the fin design was due largely to the careful modeling of the anatomy, kinematics and mechanical properties of the biological fin. The decomposition of the steady swimming movements into orthogonal modes, and subsequent CFD analysis of each mode, identified the aspects of the fin's movement and structure that were most important to swimming forces, and thus the elements that should be recreated by the robotic fin. The analysis of the mechanical properties of the fin rays and the development of a first-order scaling rule for bending allowed for the mechanical properties of the smaller, 14-rayed sunfish fin to be scaled so that the five-rayed robotic fin had a similar dynamic interaction with the fluid.

Kinematics of the robotic fin, when the fin was appropriately scaled and when tapered fins were used (Table 1, fin 3), matched closely the kinematics observed from the pectoral fin of the swimming sunfish (Fig. 2) (Lauder and Madden, 2007; Mittal et al., 2006). The key features of the biological fin that have been identified as being crucial to force generation throughout the fin stroke, especially on the outstroke, are the cupping behavior in which the dorsal and ventral edges of the fin move away from the body simultaneously, and fin flexibility which results in the distal third of the fin being bent back toward the body on the outstroke. Robotic fin 3 reproduces both of these critical behaviors, and thus this fin generates thrust throughout the fin beat cycle as does the sunfish pectoral fin. Experimental analysis of the sunfish body accelerations (Fig. 4) (Lauder and Madden, 2008) shows that there are two clear thrust peaks produced from the fin, one each on the outstroke and instroke. Furthermore, both the analysis of the fin wake (Peng et al., 2007) and computational fluid dynamic studies based on detailed sunfish pectoral fin kinematics (Dong et al., 2010) show these two thrust peaks and positive thrust throughout the fin beat cycle.

As predicted, using a first-order estimate of fin-ray deflection, fins with rays with flexural rigidities scaled to 500 to 1000 times those

of biological fin produced force traces and flow patterns that were similar to those measured and predicted for the biological fin. Notably, these fins generated positive thrust during the outstroke, whereas fins with flexural rigidities scaled above this region (2000× and 5000×) produced drag (a negative thrust). When the flexural rigidities of the robotic fin rays were within the appropriate range, peaks of thrust were produced during the outstroke and instroke, and, under certain operating conditions, thrust remained positive during the transition from the outstroke to the instroke (Figs 6 and 7). Associated with the positive thrust were fluidic jets accelerated aft by the fin to velocities faster than the freestream. Fins that were too stiff did not accelerate flow aft during the outstroke, but sideways and then forward as the outstroke progressed. DPIV results also suggested that thrust occurred during the transition when fin stiffness, flapping frequency and the speed of the water were tuned such that the fin began to straighten just before the end of the outstroke with enough speed to continue to accelerate water aft of the fin. Coupled to the positive thrust forces were lift and a ventral movement of the flow during the outstroke, and negative-lift and a dorsal movement of the flow during the instroke. The consequence of these forces would be to drive a robotic fish or underwater vehicle forward and upward during the outstroke of the fin, and forward and downward during the instroke. These are exactly the motions observed in bluegill sunfish, which, when swimming steadily in an oncoming flow, rise during the outstroke and then drop during the instroke and the delay before the subsequent fin beat (Lauder and Madden, 2008).

Our results show that a robotic pectoral fin, tuned with appropriate fin ray stiffness, taper and movements, can generate patterns of continuous thrust over a complete fin beat that do not involve periods of drag at the fin 'reversal' of motion from outstroke to instroke. These results match previous work on the flexible bluegill pectoral fin, which showed a similar phenomenon (Lauder et al., 2006; Lauder and Madden, 2007; Dong et al., 2010), and studies on patterns of body acceleration (Lauder and Madden, 2008), but stand in contrast to previous experimental or computational studies of other fish pectoral fins. For example, the wrasse pectoral fin executing a 'flapping stroke' studied by Walker and Westneat (Walker and Westneat, 2002) and Ramamurti et al. (Ramamurti et al., 2002) shows clear periods of either drag or near zero thrust for a considerable fraction of the fin beat cycle. This may be due to the rather different kinematics involved in the wrasse pectoral fin beat or to the stiffer wrasse fin, which has much less area change and spanwise flexibility than the pectoral fin of bluegill sunfish. The wrasse fin also does not display the dual leading edges and cupping behavior on the outstroke that is shown by the bluegill pectoral fin. The computational fluid–structure model of a pectoral fin by Shoele and Zhu (Shoele and Zhu, 2009) also shows a modest time of negative thrust (drag) during the reversal of the stroke. Previous robotic pectoral fin models (Kato, 2005; Palmisano et al., 2007) demonstrate periods of significant drag during the fin reversal, and no other robotic fin, to date, has been able to generate continuous thrust.

Our appropriately scaled robotic fins also looked similar to the biological fin as they were flapped in the water (Fig. 2). Differences, such as pocketing and folding of the webbing, were apparent, but did not significantly degrade the ability of the fin to produce forces and flows like those of the biological fin. As compliant as these fins were, they did not appear as deformable, or move with the same gracefulness, as the biological fins. Preliminary tests have now been conducted with tapered fin rays scaled to 200×. These fins seem to capture more of the fluidity of the biological fin, and may be further improved by increasing the number of fin rays and decreasing the thickness of the webbing.

The results of this study underscore the importance of capturing both the driven motions of the base of the biological fin and the mechanical properties of the fin's structure in a biorobotic fin model. The poor implementation of either of these biological aspects impacted adversely on the performance of the robotic fin, particularly the production of thrust during the outstroke. Previous studies using flexible fins that inaccurately produced 3-D modal movements of the biological fin failed to produce thrust during the outstroke (Tangorra et al., 2007), as did fins in this study that executed the correct trajectories at the fin base, but that were too stiff.

Although sunfish have active control over fin ray curvature (Alben et al., 2007) and can create dramatic fin shapes, the results of this study indicate that it is unnecessary to curve the fin rays actively to approximate the complex fin shapes used in steady swimming. The curvature and deformation of these highly deformable pectoral fins is largely the result of the interaction of the fluid and the fin structure. Electromyographic data on sunfish pectoral fin muscles have shown there to be co-contraction of the muscles at the base of the fin rays during some swimming behaviors (Lauder et al., 2006). This suggests active control over fin ray curvature and stiffness and may be most useful for tuning the mechanical properties of the fin for different operating conditions and to maximize forces at different times during the fin beat.

Flexural rigidity and fin-ray taper

The flexural rigidity of the fin rays, and therefore the stiffness and curvature of the fin, was a key element in the production of effective propulsive forces. Forces were created by these highly deformable fins through an exchange of energy between the fin and the surrounding fluid. As the fin moved through the water, vortices developed along the fin edges; the fin bent, stored and released energy elastically, and vortices and jets were released into the flow. These dynamics, and the magnitude and direction of the force generated by the fin, were related directly to the bending properties of the fin rays.

The peak and average magnitude of the 2-D force imparted to the water scaled directly with the stiffness of the fin rays: the stiffer the fin, the greater the magnitude of the propulsive force in the thrust-lift plane. This result held across all test conditions for the full fin beat and during the outstroke and instroke. Thus, the magnitude of the propulsive force of a fin can be modulated by actively adjusting fin-ray stiffness.

There was a more complicated relation between the thrust and lift components of the force, the flexural rigidity of the fin rays, and the portion of the fin beat during which the force was being generated. This was caused by the fact that the bending of the fin ray, and therefore the shape of the fin, affected both the magnitude of the 2-D force and the direction the force acted in the water. Thrust and lift did not always scale proportionately with fin-ray stiffness. Certainly, the stiffest of the fins (fin 3, tapered 1000×) generated more thrust and lift (Figs 8, 9) than the most compliant fins (fin 7, tapered 500×; and fin 5, uniform 600×). However, a stiffer fin did not necessarily generate more thrust and lift than a fin that was more compliant but of similar stiffness. This was evident between fins 3 (tapered 1000×) and 6 (tapered 600×), as well as between fins 3 (uniform 1000×) and 7 (tapered 500×). For almost every test condition, fin 3 produced a larger 2-D force, a larger magnitude lift during the outstroke and the instroke, and considerably larger thrust during the outstroke than did fin 6. Fin 6, however, generated significantly more thrust during the instroke than fin 3. In a sense, the spatial distribution of stiffness for fin 6 was tuned more appropriately for directing propulsive forces along the thrust axis during the instroke. Although fin 6 produced slightly less thrust than

fin 3 during the outstroke, its average thrust was similar across the fin beat, and it wasted less energy by producing high levels of lift during the outstroke that were then balanced by negative lift during the instroke.

The thrust generated during the outstroke was influenced by fin-ray stiffness, but was more sensitive to the taper of the fin ray, and therefore to the curvature of the fin as the fin moved into the flow. Fins with rays, like those of the sunfish, which tapered from a thick base to a thin tip (Alben et al., 2007), produced larger mean thrust forces during the outstroke than fins with rays that had uniform cross sections. This held for fin rays that modeled the same flexural rigidity (e.g. tapered 1000× *vs* uniform 1000×), that exhibited the same approximate total deflection (e.g. tapered 600× *vs* uniform 1000×), and even when the fin with uniform rays was stiffer and produced greater 2-D force during the outstroke (e.g. tapered 500× *vs* uniform 1000×). For fin rays that had similar total deflection, the main difference between fin rays was in how the fin ray bent. Tapered fin rays curved uniformly along their length (Fig. 5), whereas for the uniform ray the point of maximum curvature was much closer to the base of the ray and they were straighter near the tip. These results strongly suggest that the curvature of the fin rays – which define the shape of the fin, the amount of fin webbing that faces backwards, and the distribution of the energy that is stored and then released into the flow – is very influential in how forces are directed aft to create thrust during the outstroke. Among fins with rays that curved in the same manner, the average thrust scaled with the stiffness of the fin rays.

It is difficult to compare these results directly with those from studies of flexible foils because of differences in the kinematics and structure of the fin and foils. First, the 3-D rostrocaudal motions of the biorobotic fin, which exhibit an upper and lower leading edge and cupping about the spanwise axis, differ significantly from the 2-D pitch and heave motions of a flapping foil. When isolated, though, the motion of the dorsal half of the fin is somewhat similar to that of the flapping foil, in that it moves up and down and rotates through a pitch angle (Dong et al., 2010). Second, the biorobotic fin is very thin, is supported structurally by fin rays and has bending properties that vary along the chord and along the span. Studies with flapping foils have considered changes in flexibility along the chord (Katz and Weihs, 1978; Prempraneerach et al., 2003; Triantafyllou et al., 2004) and along the span (Liu and Bose, 1997), but not along both simultaneously. Also, foil shapes have usually been based on symmetric National Advisory Committee for Aeronautics (NACA) airfoils, and therefore the manner in which stiffness changed was due to the taper of the foil and was not related to properties of a biological system. However, there were some similarities between results for our biorobotic fin and those of previous work on flapping foils. First, for a fin of a particular stiffness, the magnitude of the 2-D force, and to a lesser extent thrust, increased with higher flapping frequencies and lower flow rates. Second, vortices developed along the leading edge of the fin under steady flapping, and these vortices were shed into the flow twice during the fin beat – at the end of the outstroke and instroke (Triantafyllou et al., 2004). Third, and perhaps most significantly, both studies indicate that stiffness can be tuned to maximize thrust and/or propulsive efficiency (Prempraneerach et al., 2003; Triantafyllou et al., 2004).

CONCLUSION

A biorobotic fin was developed based on biological studies of the anatomy, kinematics and hydrodynamics of the bluegill sunfish (*Lepomis macrochirus*) pectoral fin. The biorobotic fin was validated in its ability to create motions, forces and flows like the biological fin and was then used to investigate the effect of fin ray stiffness on propulsive forces over a wide range of operating conditions including variation in flapping frequency and flow rate.

Propulsive forces are created through a dynamic interaction of the fin and the water. This interaction is affected by the stiffness and geometry of the fin rays, the kinematics of the fin beat, and the flow of the fluid past the fin. When the flexural rigidities of the fin rays were scaled appropriately for the test conditions, the biorobotic fins produced force patterns that were very similar to those predicted for the sunfish: thrust and lift during the outstroke, and thrust and negative lift during the instroke. Fins that were tested with flexural rigidities outside this range produced drag (negative thrust) during the outstroke. The propulsive forces produced by each of the fins generally increased as the Strouhal number was increased – either as flow rate was decreased or as the flapping frequency of the fin was increased. The data also suggested that forces leveled off or decreased as flapping frequencies continued to rise, but the evidence to support this relationship was limited. Under the majority of conditions, the greater the stiffness of a fin, the greater the average magnitude of the 2-D propulsive force and of the lift produced during the outstroke and instroke. Thrust forces, however, did not increase directly with fin stiffness. Thrust during the outstroke was very sensitive to how fin-ray flexural rigidity changed along the length of the fin ray, and therefore to how the surface of the fin curved as the fin was swept into the oncoming flow. Thrust during the instroke tended to increase with fin stiffness, but was affected by the fact that changes to the stiffness altered both the magnitude of the 2-D force and the direction along which the force acted on the water. Incremental increases to the stiffness of the fin sometimes altered the direction of the 2-D force more than it increased the magnitude of the force, and therefore caused the thrust produced by the fin to decrease. This may be beneficial, as it means that in some situations a more compliant fin can produce greater average thrust over the fin beat than a stiffer fin, and will waste less energy than if it had produced high levels of lift during the outstroke which were then counterbalanced by negative lift during the instroke.

ACKNOWLEDGEMENTS

This work was supported by an ONR-MURI grant number N00014-03-1-0897 on fish pectoral fin function, monitored by Dr Thomas McKenna and initiated by Dr Promode Bandyopadhyay, and also by an ONR grant number N00014-09-1-0352 on fin neuromechanics. We thank members of the Tangorra, Lauder and Hunter laboratories for their advice and assistance with experiments.

REFERENCES

Alben, S., Madden, P. G. and Lauder, G. V. (2007). The mechanics of active fin-shape control in ray-finned fishes. *J. R. Soc. Interface* **4**, 243-256.

Ang, M. H., Jr, Wei, W. and Teck-Seng, L. (1993). On the estimation of the large deflection of a cantilever beam. *IECON Proc.* **3**, 1604-1609.

Bandyopadhyay, P. R. (2002). Maneuvering hydrodynamics of fish and small underwater vehicles. *Integr. Comp. Biol.* **42**, 102-117.

Belendez, T., Neipp, C. and Belendez, A. (2002). Large and small deflections of a cantilever beam. *Eur. J. Physics* **23**, 371-379.

Bozkurttas, M., Dong, H., Mittal, R., Madden, P. and Lauder, G. V. (2006). Hydrodynamic performance of deformable fish fins and flapping foils. In *AIAA 2006-1392*, Vol. 1392. Reno, NV, USA.

Bozkurttas, M., Dong, H., Mittal, R., Tangorra, J., Hunter, I., Lauder, G. V. and Madden, P. (2007). CFD based analysis and design of biomimetic flexible propulsors for autonomous underwater vehicles. In *AIAA 2007-4213*, Miami, FL, USA.

Bozkurttas, M., Mittal, R., Dong, H., Lauder, G. V. and Madden, P. (2009). Low-dimensional models and performance scaling of a highly deformable fish pectoral fin. *J. Fluid Mech.* **631**, 311-342.

Dong, H., Bozkurttas, M., Mittal, R., Madden, P. and Lauder, G. V. (2010). Computational modelling and analysis of the hydrodynamics of a highly deformable fish pectoral fin. *J. Fluid Mech.* **645**, 345-373.

Drucker, E. G. and Lauder, G. V. (1999). Locomotor forces on a swimming fish: three-dimensional vortex wake dynamics quantified using digital particle image velocimetry. *J. Exp. Biol.* **202**, 2393-2412.

Drucker, E. G. and Lauder, G. V. (2005). Locomotor function of the dorsal fin in rainbow trout: kinematic patterns and hydrodynamic forces. *J. Exp. Biol.* **208**, 4479-4494.
Fish, F. E., Nusbaum, M. K., Beneski, J. T. and Ketten, D. R. (2006). Passive cambering and flexible propulsors: cetacean flukes. *Bioinspir. Biomim.* **1**, S42-S48.
Gere, J. M. and Timoshenko, S. P. (2004). *Mechanics of Materials*, 6th edn. London: Brooks/Cole.
Gottlieb, J., Tangorra, J., Esposito, C. and Lauder, G. (2010). A biologically derived pectoral fin for yaw turn maneuvers. *Appl. Bionics Biomech.* **7**, 41-55.
Kato, N. (2005). Median and paired fin controllers for biomimetic marine vehicles. *Trans. ASME* **58**, 238-252.
Katz, J. and Weihs, D. (1978). Hydrodynamic propulsion by large amplitude oscillation of an airfoil with chordwise flexibility. *J. Fluid Mech.* **88**, 485-497.
Lauder, G. V. and Madden, P. G. A. (2007). Fish locomotion: kinematics and hydrodynamics of flexible foil-like fins. *Exp. Fluids* **43**, 641-653.
Lauder, G. V. and Madden, P. G. A. (2008). Advances in comparative physiology from high-speed imaging of animal and fluid motion. *Annu. Rev. Physiol.* **70**, 143-163.
Lauder, G. V., Madden, P. G. A., Mittal, R., Dong, H. and Bozkurttas, M. (2006). Locomotion with flexible propulsors I: experimental analysis of pectoral fin swimming in sunfish. *Bioinspir. Biomim.* **1**, S25-S34.
Lauder, G. V., Anderson, E. J., Tangorra, J. and Madden, P. G. A. (2007). Fish biorobotics: kinematics and hydrodynamics of self-propulsion. *J. Exp. Biol.* **210**, 2767-2780.
Liu, P. and Bose, N. (1997). Propulsive performance from oscillating propulsors with spanwise flexibility. *Proc. Math. Phys. Eng. Sci.* **453**, 1763-1770.
Low, K. (2009). Modelling and parametric study of modular undulating fin rays for fish robots. *Mech. Mach. Theory* **44**, 615-632.
Low, K. and Willy, A. (2006). Biomimetic motion planning of an undulating robotic fish fin. *J. Vibration Control* **12**, 1337-1359.
McHenry, M. (1995). Mechanical control of swimming speed: stiffness and axial wave form in undulating fish models. *J. Exp. Biol.* **198**, 2293-2305.
Mittal, R., Dong, H., Bozkurttas, M., Lauder, G. V. and Madden, P. (2006). Locomotion with flexible propulsors: II. Computational modeling of pectoral fin swimming in sunfish. *Bioinspir. Biomim.* **1**, S35-S41.
Oppenheim, A. V. and Schafer, R. W. (1975). *Digital Signal Processing*. Englewood Cliffs: Prentice Hall.
Palmisano, J., Ramamurti, R., Lu, K., Cohen, J., Sandberg, W. and Ratna, B. (2007). Design of a biomimetic controlled-curvature robotic pectoral fin. In *ICRA 2007*. Rome, Italy.
Peng, J., Dabiri, J. O., Madden, P. G. and Lauder, G. V. (2007). Non-invasive measurement of instantateous forcees during aquatic locomotion; a case study of the bluegill sunfish pectoral fin. *J. Exp. Biol.* **210**, 685-698.
Prempraneerach, P., Hover, F. and Triantafyllou, M. (2003). The effect of chordwise flexibility on the thrust and efficiency of a flapping foil. In *13th Int. Symp. Unmanned Untethered Submersible Techn.* Durham, NH: The Autonomous Undersea Systems Institute.
Ramamurti, R., Sandberg, W. C., Lohner, R., Walker, J. A. and Westneat, M. W. (2002). Fluid dynamics of flapping aquatic flight in the bird wrasse: three-dimensional unsteady computations with fin deformation. *J. Exp. Biol.* **205**, 2997-3008.
Shoele, K. and Zhu, Q. (2009). Fluid-structure interactions of skeleton-reinforced fins: performance analysis of a paired fin in lift-based propulsion. *J. Exp. Biol.* **212**, 2679-2690.
Standen, E. M. and Lauder, G. V. (2005). Dorsal and anal fin function in bluegill sunfish *Lepomis macrochirus*: three-dimensional kinematics during propulsion and maneuvering. *J. Exp. Biol.* **208**, 2753-2763.
Standen, E. M. and Lauder, G. V. (2007). Hydrodynamic function of dorsal and anal fins in brook trout (*Salvelinus fontinalis*). *J. Exp. Biol.* **210**, 325-339.
Tangorra, J. L., Davidson, S. N., Hunter, I. W., Madden, P. G. A., Lauder, G. V., Dong, H., Bozkurttas, M. and Mittal, R. (2007). The development of a biologically inspired propulsor for unmanned underwater vehicles. *IEEE J. Oceanic Eng.* **32**, 533-550.
Tangorra, J. L., Lauder, G. V., Madden, P. G., Mittal, R., Bozkurttas, M. and Hunter, I. W. (2008). A biorobotic flapping fin for propulsion and maneuvering. In *IEEE International Conference on Robotics and Automation 2008*, pp. 700-705. Pasadena, CA.
Triantafyllou, M., Techet, A. and Hover, F. (2004). Review of experimental work in biomimetic foils. *IEEE J. Oceanic Eng.* **29**, 585-594.
Triantafyllou, M. S., Hover, F. S., Techet, A. H. and Yue, D. K. P. (2005). Review of hydrodynamic scaling laws in aquatic locomotion and fishlike swimming. *Appl. Mech. Rev.* **58**, 226-237.
Tytell, E. D., Standen, E. M. and Lauder, G. V. (2008). Escaping flatland: three-dimensional kinematics and hydrodynamics of median fins in fishes. *J. Exp. Biol.* **211**, 187-195.
Walker, J. A. and Westneat, M. (2002). Kinematics, dynamics, and energetics of rowing and flapping propulsion in fishes. *Int. Comp. Biol.* **42**, 1032-1043.
Wilga, C. D. and Lauder, G. V. (2000). Three-dimensional kinematics and wake structure of the pectoral fins during locomotion in leopard sharks *Triakis semifasciata*. *J. Exp. Biol.* **203**, 2261-2278.
Willert, C. E. and Gharib, M. (1991). Digital particle image velocimetry. *Exp. Fluids* **10**, 181-193.
Zhu, Q. and Shoele, K. (2008). Propulsion performance of a skeleton-strengthened fin. *J. Exp. Biol.* **211**, 2087-2100.
Zhu, Q., Wolfgang, M. J., Yue, D. K. P. and Triantafyllou, M. S. (2002). Three-dimensional flow structures and vorticity control in fish-like swimming. *J. Fluid Mech.* **468**, 1-28.